Facile preparation of robust superhydrophobic surface based on multi-scales nanoparticle

Chunhong Qi[1], He Chen[1], Youyi Sun[1*], Luyan Shen[1], Xiaolin Li[1], Qiang Fu[2], Yaqing Liu[1*]

1.Shanxi Province Key Laboratory of Functional Nanocomposites, North University of China, Taiyuan 030051, P.R.China.

2. School of Civil and Environmental Engineering, University of Technology Sydney, Ultimo NSW 2007, Australia.

Abstract: A new superhydrophobic surface based on multi-scales nanoparticle was developed to improve the robustness and reproducibility. The influence of multi-scale nanoparticles on the wettability and durability of superhydrophobic surface was investigated in detail. The superhydrophobic surface with optimized composition did not only show high contact angle of 160~166.3°, but also exhibited good durability to mechanical, chemical and thermal environment. Furthermore, the superhydrophobic surface was evaluated for application in anticorrosion, anti-icing and self-cleaning. This study thus opens up an avenue for the development of robust superhydrophobic surface based on polymer nanocomposite coating for various potential applications.

Keywords: superhydrophobic coating, FEVE, micro-nanostructure, mechanical, chemical, thermal stability.

---

corresponding author: Fax: 86-351-3559669

E-mail address: syyi@pku.edu.cn (YY Sun); lyqzgz2010@163.com (YQ Liu)

1.Introduction

During the past decades, superhydrophobic surface based on polymer nanocomposite has received extensive attention due to their low-cost and facile preparation for application in corrosion protection, drag reduction, self-cleaning, oil-water separation, anti-icing, etc[1-5]. Generally, to achieve superhydrophobicity, large surface roughness of polymer nanocomposite was needed and prepared by enhancing concentration of inorganic particles[3-4]. However, these surfaces displayed low mechanical durability, such as poor wear resistance, impact resistance, or adhesion strength. The hydrophobicity of these surfaces was easily reduced under external forces. At the same time, these surfaces were also easily damaged, forming cracks, spalling and so on. Therefore, there was a great deal of efforts to enhance the mechanical durability of superhydrophobic surface via fabricating different types of particles such as various particles, doping content, multi-scales[6-9]. Among these methods, introduction of multi-scales particle was the effective method to improve the mechanical durability of superhydrophobic coatings[9]. For example, an ethanolic suspension of perfluorosilane modified multi-scale titanium dioxide (TiO_2) nanoparticles were coated on both hard and soft substrates under the assistant of adhesion agents. The coating displayed a large water contact angle (WCA) of 157.0° after finger-wipe, knife-scratch and even 40 abrasion cycles with sandpaper[10]. The 3-aminopropyltrimethoxysilane (APTES)-functionalized multi-scale silica nanoparticles (100nm and 20nm) were coated onto different substrates, forming superhydrophobic surface with a WCA of greater than 160°[11]. The composite coating composed of polydimethylsiloxane (PDMS) and multi-scale silicon dioxide (SiO_2) nanoparticles were painted on the surface of magnesium alloys, affording a superhydrophobic and mechanically robust coating, which could maintain its origin WCA (133~153°) under 50 abrasion cycles with sandpaper[12]. However, it still presents a contradiction between superhydrophobicity and mechanical durability, in which the surface with excellent superhydrophobicity still shows poor mechanical stability. As well-known, fluoroethylene vinyl ether (FEVE) has good heat-durability, wear-resistance, outstanding water-repellency, strong adherence and anti-ultraviolet[13-15]. From above respects, the coating based on multi-scale nanoparticles and FEVE maybe simultaneously exhibit excellent superhydrophobicity and mechanical durability. However, the preparation of superhydrophobic surface based on FEVE nanocomposite has been rarely studied.

Herein, we employed two different types and sized nanoparticles, 30.0nm SiO_2 and 300.0nm TiO_2 nanoparticles, and FEVE to construct composite coatings with a novel micro-nano rough surfaces. Of particular note, the SiO_2 nanoparticles were firstly modified with *N*-octyltriethoxysilane (OTS) to further enhance their compatibility to FEVE and reduce the surface energy of coating. The resultant TiO_2/SiO_2/FEVE nanocomposite coatings do not only show good superhydrophobicity, but also possess good thermal and mechanical stability. This study is expected to introduce an effective approach for preparing durable superhydrophobic coatings for various practical applications.

2. Experimental

2.1 Materials

Silica (D=30 nm) and TiO_2 (D=300 nm) were purchased from Beijing deke daojin technology co. Ltd. Fluoroethylene vinyl ether (FEVE) and curing agent were purchased from Shanxi Dongfanghong Paint Co., Ltd. Xylene was purchased from Tianjin guangfu technology development Co., Ltd. Q235 and transparent glass slides were purchased from the local chemical market. All reagents were used without further purification.

2.2 Chemical modification of SiO_2 nanoparticles

The SiO_2 nanoparticles were modified with *N*-octyltriethoxysilane (OTS) as shown in Scheme 1. Firstly, 10 g SiO_2 nanoparticle was dispersed in 100 mL toluene to form a homogeneous dispersion. Then, 10 mL OTS was added into the mixture and stirred continuously at 120℃ for 12h. After then, the reaction mixture was cooled to room temperature and washed with toluene and ethanol for several times. The hydrophobic SiO_2 nanoparticles were dryed at 65℃.

Scheme 1.

2.3 Preparation of TiO_2/SiO_2/FEVE nanocomposite coating

The TiO_2/SiO_2/FEVE nanocomposite coating was prepared via a simple spraying method. Firstly, a certain amount of modified SiO_2 and TiO_2 was dispersed in xylene at room temperature and sonicated for 10.0min to form a uniform dispersion. Typically, FEVE and curing agent were dispersed in xylene under ultrasonication for 10.0min and the mass ratio of FEVE to the curing agent was 10:1. Then, the modified dispersion was added into the mixture of FEVE and curing agent to form the paint. Finally, this paint based on nanoparticles and FEVE was spray-coated on the substrates and then cured at room temperature for 24h. A series of coatings were

fabricated by varying the proportions of SiO_2 and TiO_2 (i.e. 1.5:3 and 2:3).

2.4 Instruments and characterization

The morphology of the obtained samples was observed by Field emission scanning electron microscopy (SEM, Su-8010) and metallographic microscope (IM300).

Static WCA and sliding angles (CA) were measured at ambient temperature using an optical contact angle meter (DSA100, Germany) and the volume of droplets was 5 and 10.0μL, respectively.

The tape and peel tests were conducted by ASTM D 3359-09 and GB/T 5210-2006, respectively to measure adhesion strength of coating with the substrates.

The impact resistance was performed according to GB/T1732-1993 by falling weight test. The impact energy (*E*, J) was further calculated to evaluate the impact resistance as shown in following.

E=m·g·H

Where, m, g and H are the mass of the impinging ball (1.0Kg), the gravity (9.81 m/s^2) and the height of the weight fall, respectively. The impact height was successively increased in 5-cm-steps and 1-cm-step. All impact sites were visually evaluated by means of an optical stereo microscope at 10.0 magnification. The failure criterion was the impact energy value (in J) that caused radial cracking in the coating system.

3. Results and Discussion

The micro-structure and WCA of FEVE coating, TiO_2/FEVE composite coating and TiO_2/SiO_2/FEVE composite coating were characterized and compared as shown in Fig.1. As shown in Fig.1A, the pristine FEVE coating showed a relatively smooth surface and lots of cracks. As expected, the pristine FEVE coating displayed a small WCA of 88.3°, indicating a hydrophilicity as shown in inset of Fig.1A. After doping 30wt% TiO_2 particles (D~300nm) into FEVE matrix, the composite coating still showed a relatively smooth surface, yet it showed few cracks. These results indicated that the TiO_2 particles could improve the film formation of FEVE resin, meanwhile suppress the formation the cracks. As shown in Fig.1C, the surface roughness of composite coating obviously increased, which was attributed to the synergistic effect of 15wt% SiO_2 (30nm in diameter) and 30wt% TiO_2 nanoparticles (300nm in diameter). After introduction of TiO_2 and modified SiO_2 nanoparticles, the composite coatings exhibited an larger WCA than 90.0°, suggesting a hydrophobic nature as

shown in inset of Fig.1B and 1C. When the content of SiO_2 nanoparticles was further improved to 20wt%, the surface of composite coating clearly showed porous structure, leading to a greater surface roughness. The composite coating with 30wt% TiO_2 and 20wt% SiO_2 showed the biggest WCA of 166.3° as shown in inset of Fig.1D, indicating a surperhydrophobicity. On a rough hydrophobic surface, the WCA follows the Cassie-Baxter equation (1), which is theoretically positively related to the air fraction (f) in the composite surface.

$$\cos\theta_c = f(\cos\theta_0 + 1) - 1 \qquad (1)$$

Where θ_c and θ_0 are the WCA of water droplets on the rough and smooth surfaces with the same chemical composition, respectively. f is the fraction of solid-liquid contact area. The micro-nano surface structure is conducive to produce a higher surface roughness, so that more air can be captured as shown in Fig.2F. The air layer can serve as a physical barrier to reduce the contact area of water droplets and the surface. Together with the low surface energy derived from OTS, the surface can achieve excellent superhydrophobicity(166.3°).

Fig.1.

At present, the superhydrophobic surface with micro and/or nano coarse structures are usually easy to be destroyed by mechanical forces, thus losing their superhydrophobicity. In order to solve this tough problem, we chose FEVE resin with good film-forming and bonding properties as a binder, which greatly improved the bonding strength between the coating and substrate. Here, the tape method was firstly performed to evaluate adhesion of composite coating with metal substrate as shown in Fig.2A-D. According to ASTM D3359, it ranged from 0B (complete removal of coating film lattices) to 5B (intact lattices with completely smooth edges)[17]. Visible detachment of pristine FEVE coating after the tape test was clearly observed as shown in Fig.2A, indicating a adhesion level of 3B between FEVE coating and metal substrate based on the descriptive scale. As shown in Fig.2B-D, the intact lattices with completely smooth edges was observed for the composite coatings, indicating the highest adhesion level of 5B. The adhesion level of composite coating was obviously improved from 3B to 5B, indicating a stronger adhesion of composite coating with substrate comparing to pure FEVE coating. The result was attributed to that the inorganic particles could improve mechanical strength of FEVE segments. Of particular, the composite coatings still maintained their superhydrophobicity after tape

test as shown in inset of Fig.2D. The adhesion between coating and substrate was further detected by peel tests as shown in Fig.2E-H. The adhesion strength between pristine FEVE and substrate was only about 3.2MPa. After the introduction of TiO_2 particles, the adhesion strength was greatly improved to 14.0MPa. Although this value slightly decreased from 14.0MPa to 8.9MPa when introducing 20wt% SiO_2 nanoparticles, the composite coating still possessed large adhesion strength with metal substrates. As well-known, the adhesion strength between coating and substrate was mainly attributed to polymer matrix. Generally, the polymer coating with larger mechanical strength showed adhesion strength. So, the TiO_2/FEVE coating showed larger adhesion strength comparing to pure FEVE coating. However, when the content of inorganic particles was further increased, these inorganic particles replaced the FEVE to contact with substrate. At the same time, the mechanical strength was decreased due to aggregate of inorganic particles. So, it showed a decrease of adhesion strength after introduction of more SiO_2 nanoparticles.

Fig.2.

The impact resistance of various coatings was characterized and compared by falling weight test as shown in Fig.3. After the falling weight test, the damage morphology of pristine FEVE coating were displayed in Fig.3B(a). It clearly showed lateral cracking and severe coating detachment at the impact edge, indicating a poor impact resistance of ~0.98J (corresponding to 10.0cm height). In contrast, these composite coatings showed plastic deformation and few visible cracks as shown in Fig.3B-D. In addition, the impact energy of composite coating based on TiO_2 was dramatically improved from 0.98J to 8.72J (corresponding to 89 cm height) as shown in Fig.3A. At the same time, it was found that the impact energy of the composite coating slight decreased to 6.96J (corresponding to 71.0cm height) after the incorporation of SiO_2 nanoparticles. These results were attributed to the reinforcing effect of TiO_2 and SiO_2, agreeing well with the results obtained from adhesion tests. A proper amount of SiO_2 could work synergistically with TiO_2 to form a uniform and effective network structure in the matrix, thus maintaining excellent impact resistance.

Fig.3.

Importantly, the bending experiments were also tested to further verify aforementioned mechanical stability of the composite coating with 30wt% TiO_2 and 20wt% SiO_2 as shown in Fig.4. The glass rod with a radius (R) of 7.0mm was used as the bending center and the angle between the bent coating and the horizontal plane

was defined as the bending angles θ and -θ as shown in Fig.4A. The corresponding WCA was recorded after bending tests at different angles as shown in Fig.4B-C. The WCA of composite coating was larger than 160° after bending at different angles. This result indicated that the composite coating could maintain excellent superhydrophobicity at different bending increments. In addition, the bending angle from -90° (maximum downward bending) to 90° (maximum upward bending) was defined as a bending cycle, and the WCA of composite coating was measured as a function of the bending cycles. It was found that the composite coating still showed a large WCA of 156.0° after 30 bending cycles as shown in Fig.4D. As shown in Fig.4E, no cracks were observed on the surface of composite coating after 30 bending cycles. These results further demonstrated the presented composite coatings with excellent bending resistance, flexibility, adhesion ability and mechanical durability.

Fig.4.

The sandpaper abrasion test was carried out to examine the wear resistance of composite coating with 30wt% TiO_2 and 20wt% SiO_2 as shown in Fig.5. Fig.5A showed the schematic illustration of the sandpaper abrasion test. The coating was placed face-down to sandpaper (standard glasspaper, grit no. 240) under a load of 100g and moved for 10cm, followed by rotated by 90° and moved for another 10cm. We defined this process as one abrasion cycle, ensuring both longitudinal and transverse friction could be carried out simultaneously during the friction process of each cycle. As shown in Fig.5B, the WCA and the sliding angle of composite coating slightly decreased from 166.3° to 158.6° and increased from 1.0° to 14.0° after 50 abrasion cycles, respectively. The result indicated that the superhydrophobicity of composite coating was reserved under mechanical wear. The water drop on composite coating before and after 50 abrasion cycles was slight change as shown in inset of Fig.5B. The surface structure of composite coating before and after friction was also characterized and compared by the SEM images as shown in Fig.5C and 5D, respectively. The composite coating before and after friction obviously displayed similar surface morphology. These results demonstrated the presented composite coatings with excellent wear resistance. The good wear resistance was attributed to relatively small surface roughness and the incorporation of micro size particles with excellent wear resistance.

Fig.5.

The thermal stability of the presented composite coating was investigated by thermogravimetry instrument at a heating rate of 10°C/min in air. As shown in Fig.6A, a bit weight loss of composite coating was observed below 300°C, suggesting excellent thermal stability below 300°C. When the temperature increased over 300°C, the weight loss of composite coating increased to ca. 40wt%, resulting from the thermal degradation of FEVE resin. In addition, this result agreed well with the doping content of SiO_2 and TiO_2 particles (totally ca. 50wt%) in FEVE matrix. The WCA of composite coating as a function of treatment temperature was also characterized as shown in Fig.6B. The composite coating was heated in a muffle furnace at 50°C~400°C for 3 hours. It was found that the WCA of composite coating maintained around 155.0° below 300°C. When the treatment temperature increased over 350°C, the WCA dramatically decreased to close 0°. This result was attributed to the decomposition of FEVE. These results demonstrated that the composite coating had excellent thermal stability from 25°C to 300°C.

Fig.6.

The self-cleaning property of various coatings was characterized and compared as shown in Fig.7. It was clearly observed that the contaminant particles could be easily removed from the composite coating with 30wt% TiO_2 and 20wt% SiO_2 nanoparticles by the rolled water droplets. In this process, the surface of the inclined coating was completely cleaned as shown in Fig.7A. The good self-cleaning property of the composite coating was mainly attributed to the superhydrophobic surface, forming air film. Such air film could effectively reduce the direct contact between the contaminant and the coating. Thus, when water droplets passed through the surface, the contaminants were carried away. Fig.7E showed the WCA of the composite coating as a function of self-cleaning cycles. In the experiment, methyl orange was used to simulate dust to help visualization. It was found that the dust on the coating could be completely removed after 50 cycles. In contrast, the contaminant particles were difficult to be removed from other coatings by the rolled water droplets (in Fig.7B-D). The result was attributed to the low hydrophobicity of other coatings. These results strongly indicated that the presented composite coatings with with 30wt% TiO_2 and 20wt% SiO_2 had excellent self-cleaning ability.

Fig.7.

The anti-icing ability of various coatings was also evaluated and compared by using high-speed camera as shown in Fig.8. It was found that the ice was grown from

bottom to the top after a cooling period. When the water began to freeze, the transparent center of the condensed water vanished due to the difference in reflectivity between water and ice. It clearly showed that the froze time and and precooling time of water droplet on pristine FEVE coating was about 69s and 30s at -25℃, respectively as shown in Fig.8A. In contrast, the froze time and precooling time of water droplet on composite coating with 30wt% TiO_2 and 20wt% SiO_2 was prolonged to 389s and 215s, respectively as shown in Fig.8D. In general, these results were mainly caused by the following three reasons. Firstly, the composite coating with 30wt% TiO_2 and 20wt% SiO_2 could provide superhydrophobic surface,greatly reducing the contact area between droplets and the coating surface[18-19]. Secondly, the large amount of air layer trapped in the superhydrophobic surface acted as a good insulation layer to prevent the droplets from freezing, thus delaying the time when the droplets reached the nucleation temperature. Finally, the composite coating showed small surface roughness, providing good free-energy barrier and delaying the formation of ice nucleation. These results indicated that the present composite superhydrophobic coating with 30wt% TiO_2 and 20wt% SiO_2 had good anti-icing ability.

Fig.8.

Superhydrophobic coating was considered to be an effective metal anticorrosion method due to its excellent water repellency. Here, the anticorrosion of various coatings were characterized and compared by Tafel polarization curves in the 3.5wt% NaCl solutiou as shown in Fig.9A. The values of corrosion current densities (I_{corr}), corrosion potentials (E_{corr}), polarization resistance (R_p) and corrosion rate (V_{corr}) were calculated according the Tafel polarization curves as shown in Table 1. It clearly showed that the E_{corr} was shifted towards positive direction with increasing in hydrophobic performance as shown in Fig.9A. Specifically, the E_{corr} of composite coating with 30wt% TiO_2 and 20wt% SiO_2 covered Fe was shifted positively for about 0.67V comparing with the pristine FEVE coated Fe. This suggested that the composite coating with 30wt% TiO_2 and 20wt% SiO_2 could retard the dissolution of Fe from seawater due to superhydrophobicity [20]. In addition, the I_{corr}, and V_{corr} values of coatings covered metal decreased with increasing their hydrophobicity as shown in Table 1. The I_{corr}, and V_{corr} values of composite coating with 30wt% TiO_2 and 20wt% SiO_2 covered Fe both decreased by about two orders of magnitude comparing with that of pristine FEVE coated Fe. It was well-known that the lower I_{corr}

or V_{corr} showed better anticorrosive performance[21-22]. In other words, the composite coating with 30wt% TiO_2 and 20wt% SiO_2 showed best anticorrosion comparing to other coatings. Above result was further confirmed by the Nyquist plots as shown in Fig.9B. All samples displayed a semicircle at high frequency, which represented the charge transfer resistance (R_{ct}) at the metal/solution interface. A larger semicircle suggested a higher R_{ct} value, meaning a longer path of the ion diffusion from aqueous solution to metal substrate. The R_{ct} values obviously increased with increasing in hydrophobicity of coating. Specifically, the R_{ct} of composite coating with 30wt% TiO_2 and 20wt% SiO_2 covered Fe was about 410K$\Omega \cdot cm^2$, which was 10 times higher than that of the pristine FEVE coating covered Fe. Generally, a larger R_{ct} value indicated a lower corrosion rate [23]. The result further indicated the good anticorrosion performance of composite coating with 30wt% TiO_2 and 20wt% SiO_2. The result was attributed to superhydrophobicity, capturing a lot of air and forming a stable air film on composite coating. The air layer could effectively prevent the diffusion of corrosive Cl^- ions from water to substrate. In addition, the FEVE resin with good barrier to corrosive Cl^- ions was also key role for the excellent anticorrosion.

Fig.9.

Table 1.

4.Conclusions

In summary, a novel superhydrophobic coating based on multi-scale nanoparticles was developed and prepared by one-step spray-coating. The superhydrophobic coating with multi-scale structure did not only exhibit good superhydrophobicity, but also possessed excellent mechanical and thermal stability. Furthermore, the presented coatings showed good self-cleaning, anti-icing and anticorrosion performance. This work provides a new approach to improve durability of superhydrophobic surface, which has great potential in various practical applications.

Acknowledgments

The authors are grateful for the support of the National Natural Science Foundation of China under grants (51773184 and U1810114), and Shanxi Provincial Natural Science Foundation of China (201701D121046 and 201803D421081).

Reference

[1]Y.Ye, D.Zhang, J.Li, T.Liu, J.Pu, H.Zhao, L.Wang, One-step synthesis of

superhydrophobic polyhedral oligomeric silsesquioxane-graphene oxide and its application in anti-corrosion and anti-wear fields, Corrosion Science, 147 (2019) 9-21.

[2]G.B. Hwang, A. Patir, K. Page, Y. Lu, E. Allan, I.P. Parkin, Buoyancy increase and drag-reduction through a simple superhydrophobic coating, Nanoscale, 9 (2017) 7588-7594.

[3]W.S.Wong, Z.H.Stachurski, D.R.Nisbet, A.Tricoli, Ultra-Durable and Transparent Self-Cleaning Surfaces by Large-Scale Self-Assembly of Hierarchical Interpenetrated Polymer Networks, ACS applied materials & interfaces, 8 (2016) 13615-13623.

[4]J.Lv, XQ.Yin, R.G.Li, J.H. Chen, Q.Lin, L. Zhu, Superhydrophobic PCL/PS composite nanofibrous membranes prepared through solution blow spinning with an airbrush for oil adsorption, Polymer Engineering & Science, 59(2018)E171-E181.

[5]Z.Q.Yuan, J.P. Bin, X.Wang，Q.L.Liu, D.J. Zhao, H. Chen, H.Y. Jiang, Preparation and anti-icing property of a lotus-leaf-like superhydrophobic low-density polyethylene coating with low sliding angle, Polymer Engineering & Science, 52(2012)2310-2315.

[6]Y.Zhang, L.Zhang, Z.Xiao, S.Wang, X.Yu, Fabrication of robust and repairable superhydrophobic coatings by an immersion method, Chemical Engineering Journal, 369 (2019) 1-7.

[7]D.Zhi, Y.Lu, S.Sathasivam, I.P.Parkin, X.Zhang, Large-scale fabrication of translucent and repairable superhydrophobic spray coatings with remarkable mechanical, chemical durability and UV resistance, Journal of Materials Chemistry A, 5 (2017) 10622-10631.

[8]W.Peng, X.Gou, H.Qin, M.Zhao, X.Zhao, Z.Guo, Robust $Mg(OH)_2$/epoxy resin superhydrophobic coating applied to composite insulators, Applied Surface Science, 466 (2019) 126-132.

[9]Z.Cui, L.Yin, Q.Wang, J. Ding, Q.Chen, A facile dip-coating process for preparing highly durable superhydrophobic surface with multi-scale structures on paint films, J Colloid Interface Sci, 337 (2009) 531-537.

[10] H.Wang, F.Sun, C.Wang, Y.Zhu, H.Wang, A simple drop-casting approach to fabricate the super-hydrophobic PMMA-PSF-CNFs composite coating with heat-, wear- and corrosion-resistant properties, Colloid and Polymer Science, 294 (2015) 303-309.

[11]R.G.Karunakaran, C.H.Lu, Z.Zhang, S.Yang, Highly transparent superhydrophobic surfaces from the co-assembly of nanoparticles (≤100nm), Langmuir : the ACS journal of surfaces and colloids, 27 (2011) 4594-4602.

[12]J.Xie, J.Hu, X.Lin, L.Fang, F.Wu, X.Liao, H.Luo, L.Shi, Robust and anti-corrosive PDMS/SiO_2 superhydrophobic coatings fabricated on magnesium alloys with different-sized SiO_2 nanoparticles, Applied Surface Science, 457 (2018) 870-880.

[13]Y.Wu, X.Li, C.Mi, L.Zong, X.Wang, Preparation and characterization of perfluorine-SiO_2 nanoparticles and superhydrophobic fluorosilicone/silica hybrid composite coating, Applied Physics A, 125 (2019).

[14]J.Zhang, C.Li, K.Yan, L.Shen, N.Bao, Influence of the Aspect Ratio of Sodium Iron Titanate Whiskers on the Mechanical and Tribological Performances of Fluorocarbon Composite Coatings, Coatings, 9 (2019) 683.

[15]Y.Zhou, MLi, X.Zhong, Z.Zhu, P.Deng, H.Liu, Hydrophobic composite coatings with photocatalytic self-cleaning properties by micro/nanoparticles mixed with fluorocarbon resin, Ceramics International, 41 (2015) 5341-5347.

[16]Y.Shen, H.Tao, S.Chen, Y.Xie, T.Zhou, T.Wang, J.Tao, Water repellency of hierarchical superhydrophobic Ti6Al4V surfaces improved by secondary nanostructures, Applied Surface Science, 321 (2014) 469-474.

[17]D.Kumar, L.Li, Z.Chen, Mechanically robust polyvinylidene fluoride (PVDF) based superhydrophobic coatings for self-cleaning applications, Progress in Organic Coatings, 101 (2016) 385-390.

[18]Y.Li, B.Li, X.Zhao, N.Tian, J.Zhang, Totally Waterborne, Nonfluorinated, Mechanically Robust, and Self-Healing Superhydrophobic Coatings for Actual Anti-Icing, ACS applied materials & interfaces, 10 (2018) 39391-39399.

[19]X.Zhan, Y.Yan, Q.Zhang, F.Chen, A novel superhydrophobic hybrid nanocomposite material prepared by surface-initiated AGET ATRP and its anti-icing properties, J. Mater. Chem. A, 2 (2014) 9390-9399.

[20]A.C.de Leon, R.B.Pernites, R.C.Advincula, Superhydrophobic colloidally textured polythiophene film as superior anticorrosion coating, ACS applied materials & interfaces, 4 (2012) 3169-3176.

[21]K.Cai, S.Zuo, S.Luo, C.Yao, W.Liu, J.Ma, H.Mao, Z.Li, Preparation of polyaniline/graphene composites with excellent anti-corrosion properties and their application in waterborne polyurethane anticorrosive coatings, RSC Adv., 6 (2016)

95965-95972.
[22]M.Cui, Y.Shen, H.Tian, Y.Yang, H.Feng, J.Li, Influence of water adhesion of superhydrophobic surfaces on their anti-corrosive behavior, Surface and Coatings Technology, 347 (2018) 38-45.
[23]H.Hu, Y.He, Z.Long, Y.Zhan, Synergistic effect of functional carbon nanotubes and graphene oxide on the anti-corrosion performance of epoxy coating, Polymers for Advanced Technologies, 28 (2017) 754-762.

Table 1. Analysis results of Tafel polarisation curves and electrochemical impedance spectroscopy of various coatings covered metal after immersion in a 3.5wt% NaCl aqueous solution.

Scheme 1. Schematic illustration of the fabrication processes for modified SiO_2 nanoparticles.

Fig.1 SEM images of the various coatings, (A) pure FEVE, (B) FEVE with 30wt% TiO_2 (300.0nm), (C) FEVE with 30wt% TiO_2 (300.0nm) and 15wt% SiO_2 (30.0nm), (D) FEVE with 30wt% TiO_2 (300.0nm) and 20wt% SiO_2 (30.0nm). (E) and (F) are the schematic diagram of composite coating with TiO_2 and TiO_2/SiO_2, respectively.

Fig.2. Optical photographs of various coatings after (A-D) tape and (E-H) peel test. (A, E) pure FEVE, (B, F) FEVE with 30wt% TiO_2 (300.0nm), (C, G) FEVE with 30wt% TiO_2 (300.0nm) and 15wt% SiO_2 (30.0nm), (D, H) FEVE with 30wt% TiO_2 (300.0nm) and 20wt% SiO_2 (30.0nm).

Fig.3. (A) The impact energy and (B) optical photographs of various coatings after impact resistance test, (a) pure FEVE, (b) FEVE with 30wt% TiO_2 (300.0nm), (c) FEVE with 30wt% TiO_2 (300.0nm) and 15wt% SiO_2 (30.0nm), (d) FEVE with 30wt% TiO_2 (300.0nm) and 20wt% SiO_2 (30.0nm). Optical microscope of red part in composite coating with (C) 30wt% TiO_2 (300.0nm) and (D) 30wt% TiO_2/20wt% SiO_2.

Fig.4. (A) Schematic illustration of bending test, (B) the WCA and (C) optical photographs of composite coating after bending at different angles, (D) the WCA of composite coatings as function of bending cycles, (E) SEM image of composite coatings after 30 bending cycles. The insets of (B) and (D) are the digital image of water droplet on coating.

Fig.5. (A) Schematic illustration of the sandpaper abrasion test, (B) WCA of composite coating as function of abrasion cycles, The SEM images of composite coating (C) before and (D) after friction, The insets of (B) are digital image of water droplets on the corresponding coating and profile images of the WCA of corresponding coating before and after 50 abrasion cycles.

Fig.6. (A) The TG curve of composite coating, (B) WCA of composite coating as function of treatment temperatures for 3h.

Fig.7. Optical photograph of the self-cleaning process on various coatings, (A) FEVE with 30.0wt% TiO_2 (300.0nm) and 20.0wt% SiO_2 (30.0nm), (B) FEVE with 30.0wt% TiO_2 (300.0nm) and 15.0wt% SiO_2 (30.0nm), (C) FEVE with 30.0wt% TiO_2

(300.0nm), (D) pure FEVE. (E) WCA of composite coating as function of self-cleaning cycles. The insets of (E) are the optical photograph of the 50th self-cleaning process on composite coatings.

Fig.8. Optical photograph of water droplet on various coatings at -25.0°C, (A) pure FEVE, (B) FEVE with 30.0wt% TiO_2 (300.0nm), (C) FEVE with 30.0wt% TiO_2 (300.0nm) and 15.0wt% SiO_2 (30.0nm), (D) FEVE with 30.0wt% TiO_2 (300.0nm) and 20.0wt% SiO_2 (30.0nm).

Fig.9. (A) Tafel polarization curves and (B) Nyquist plots of various coatings covered metal, (a) pure FEVE, (b) FEVE with 30.0wt% TiO_2 (300.0nm), (c) FEVE with 30.0wt% TiO_2 (300.0nm) and 15.0wt% SiO_2 (30.0nm), (d) FEVE with 30.0wt% TiO_2 (300.0nm) and 20.0wt% SiO_2 (30.0nm).

Table 1.

Sample	Contact angle	E_{corr} (V)	I_{corr} (A/cm^2)	R_p (MΩ cm^2)	R_{ct} (KΩ cm^2)	V_{corr} (mm/year)
FEVE	88.3	-0.92	5.25×10^{-8}	1.42×10^{3}	67.87	16.95×10^{-4}
FEVE/TiO_2	92.6	-0.61	1.02×10^{-8}	4.78×10^{3}	76.06	3.29×10^{-4}
FEVE/TiO_2(30)/ SiO_2(15)	131.7	-0.38	3.20×10^{-9}	1.09×10^{4}	179.3	1.03×10^{-4}
FEVE/TiO_2(30)/ SiO_2(20)	166.3	-0.25	2.61×10^{-10}	4.1×10^{5}	410	8.44×10^{-6}

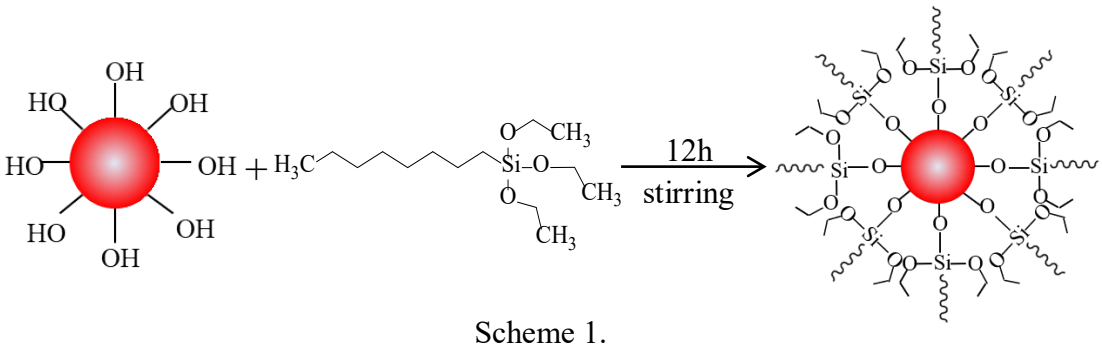

Scheme 1.

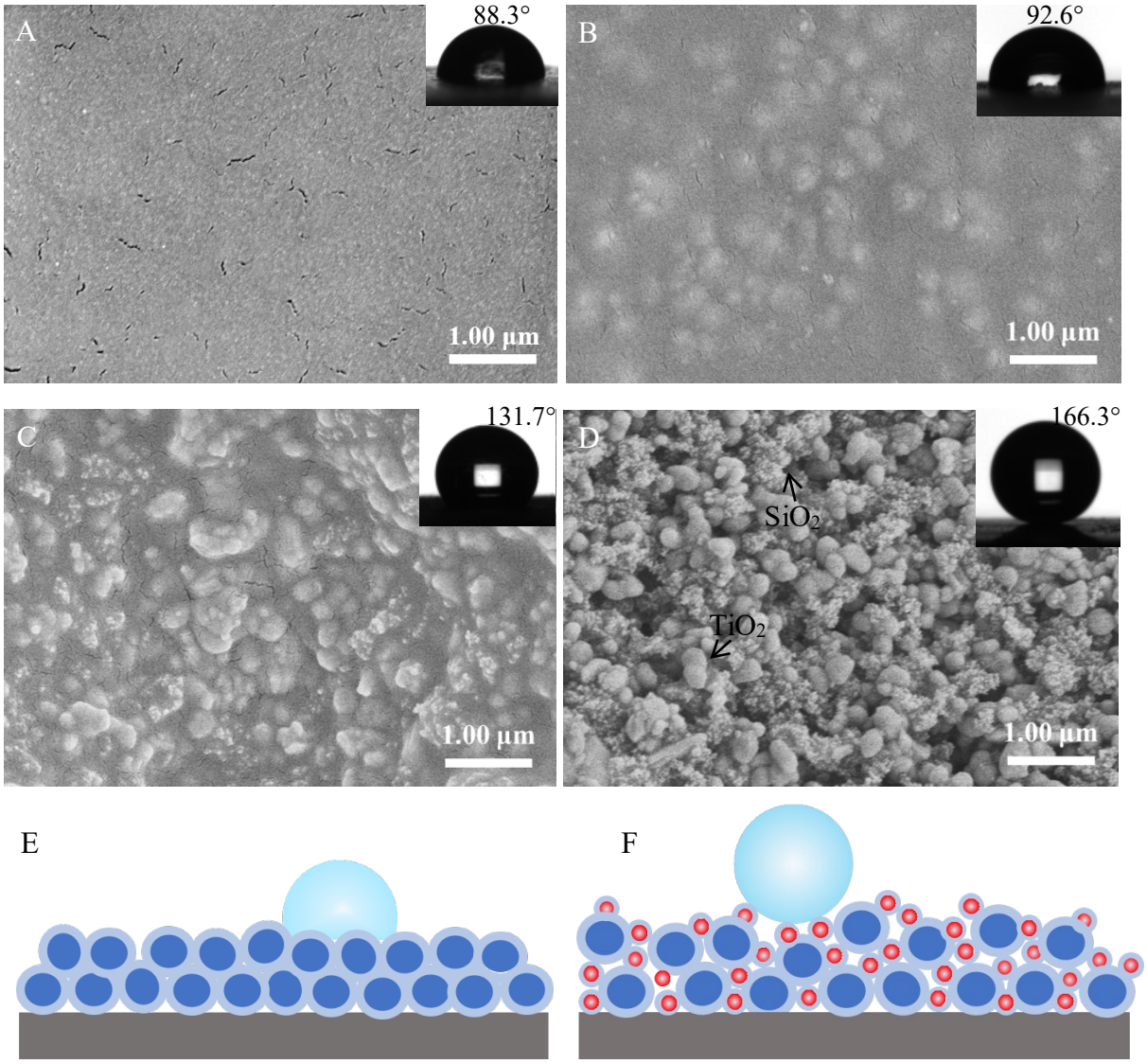

Fig.1.

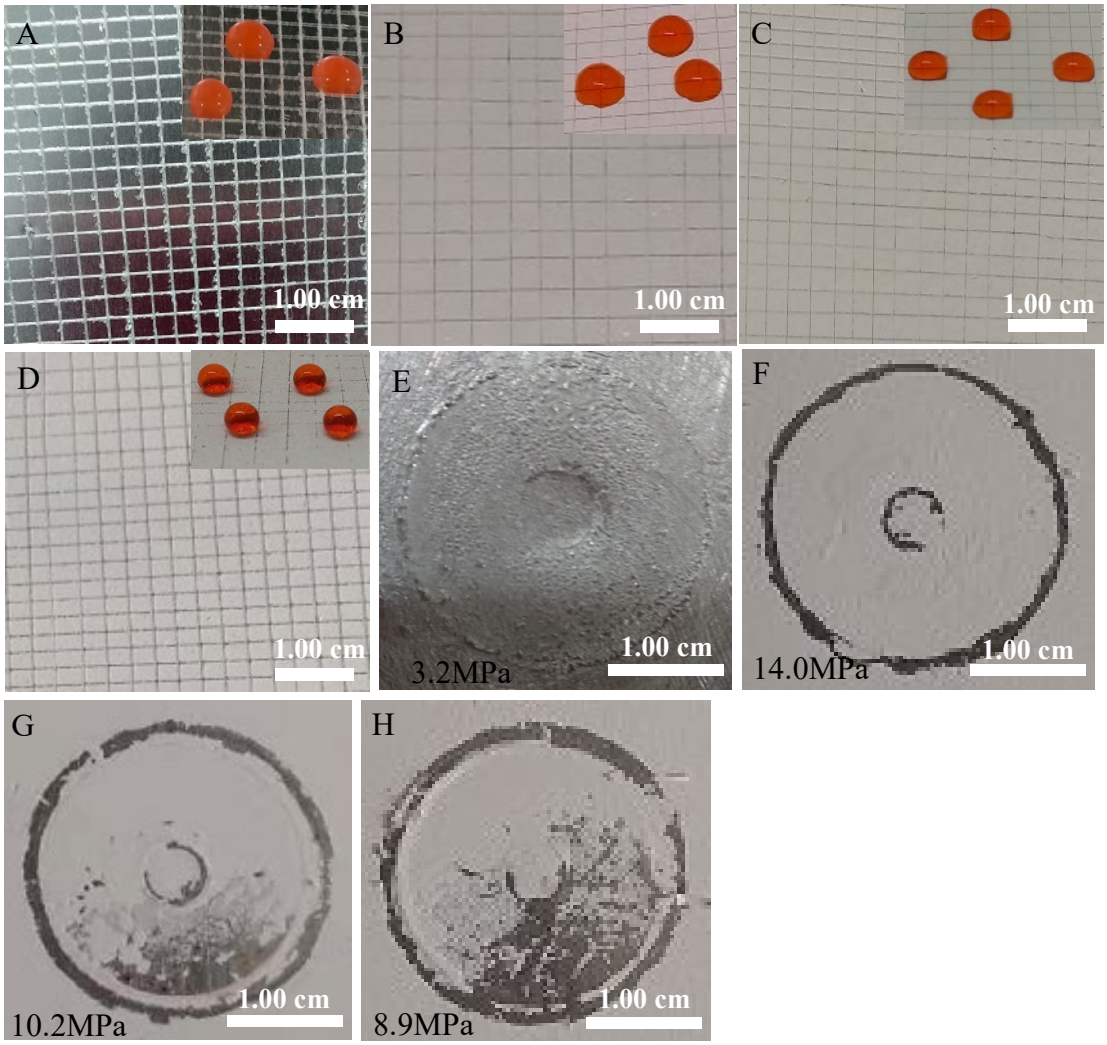
A
1.00 cm
B
1.00 cm
C
1.00 cm
D
1.00 cm
E
3.2MPa
1.00 cm
F
14.0MPa
1.00 cm
G
10.2MPa
1.00 cm
H
8.9MPa
1.00 cm

Fig.2.

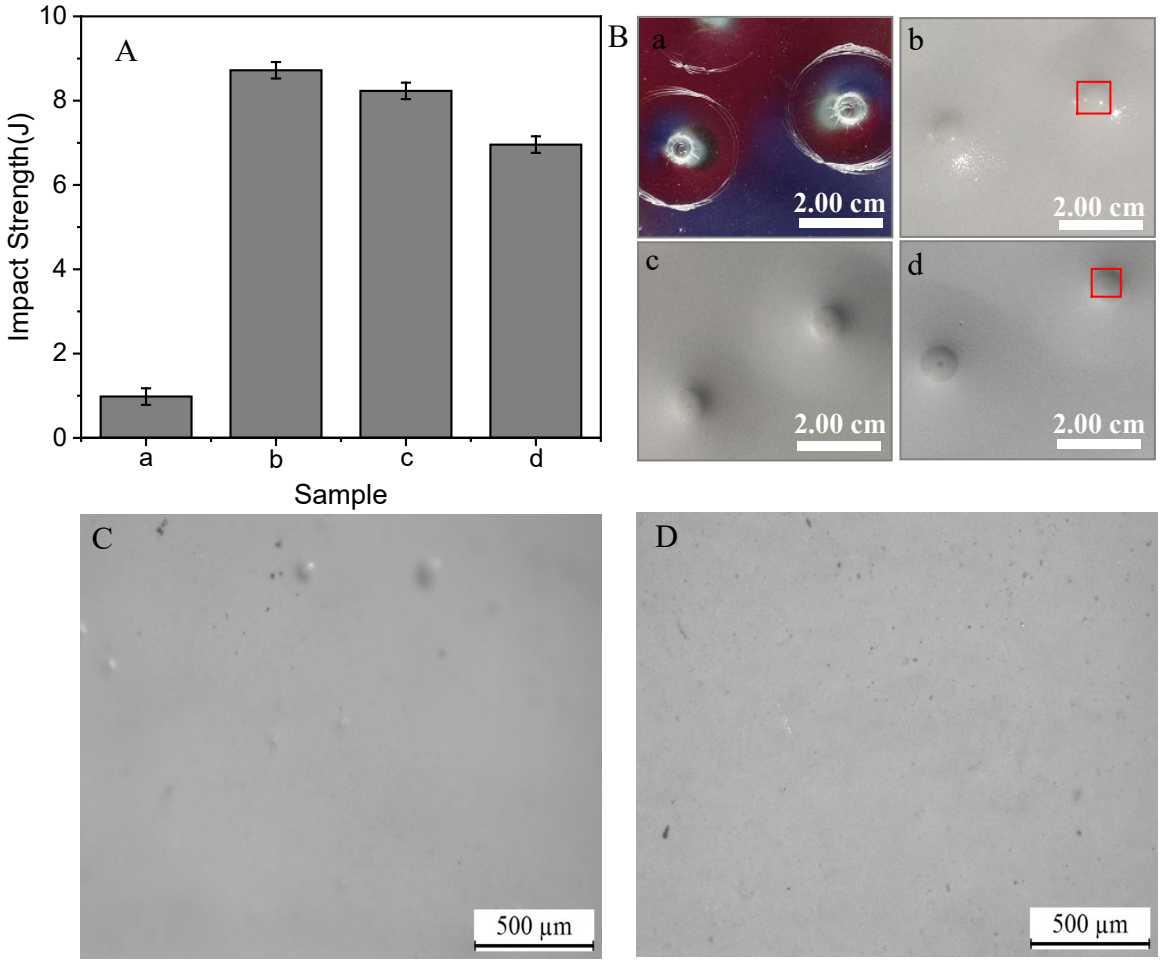
A
Impact Strength(J)
10
8
6
4
2
0
a
b
c
d
Sample
B
a
2.00 cm
b
2.00 cm
c
2.00 cm
d
2.00 cm
C
500 μm
D
500 μm

Fig.3.

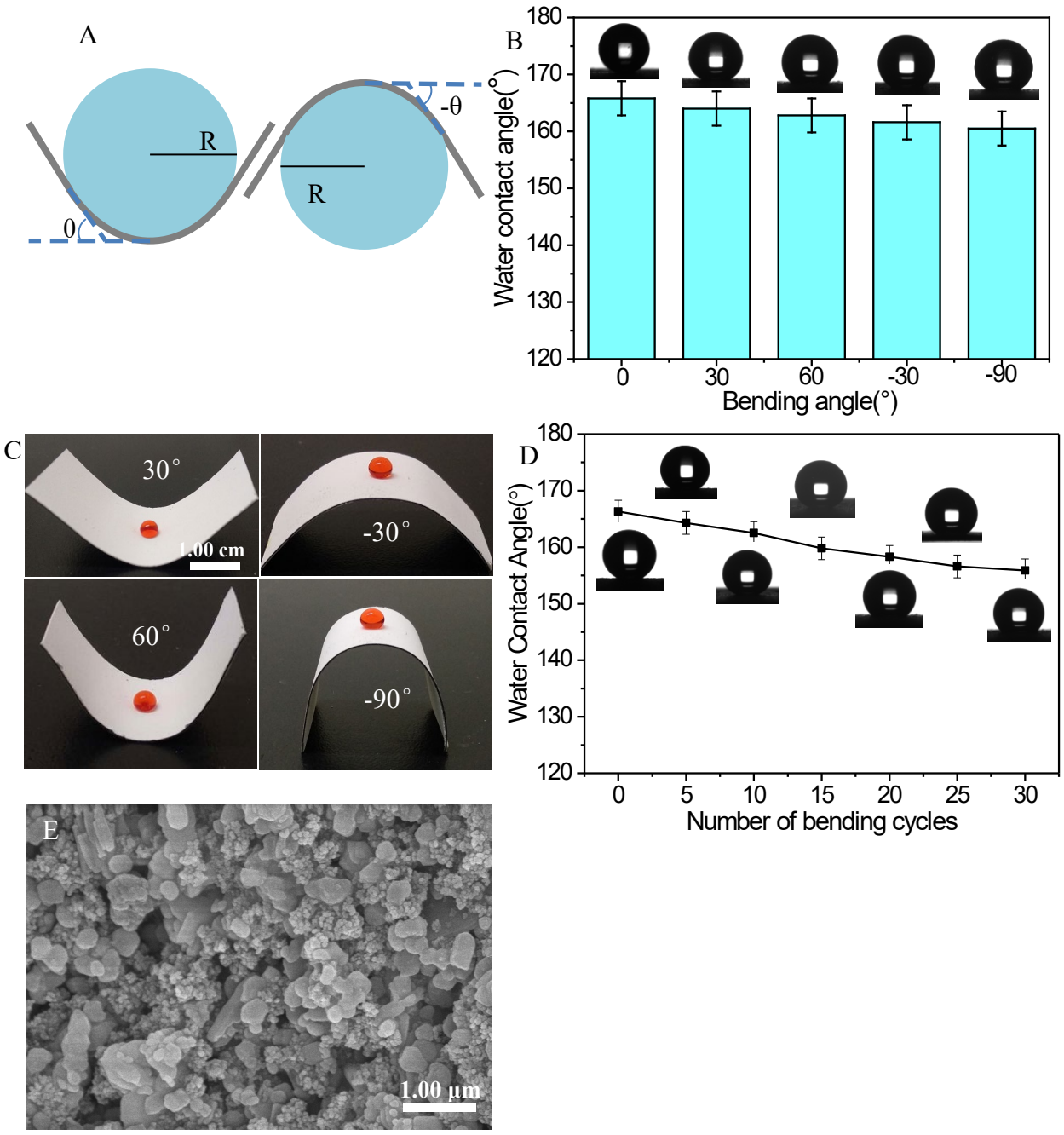
A
R
R
θ
-θ
B
Water contact angle(°)
180
170
160
150
140
130
120
0
30
60
-30
-90
Bending angle(°)
C
30°
1.00 cm
-30°
60°
-90°
D
Water Contact Angle(°)
180
170
160
150
140
130
120
0
5
10
15
20
25
30
Number of bending cycles
E
1.00 μm

Fig.4.

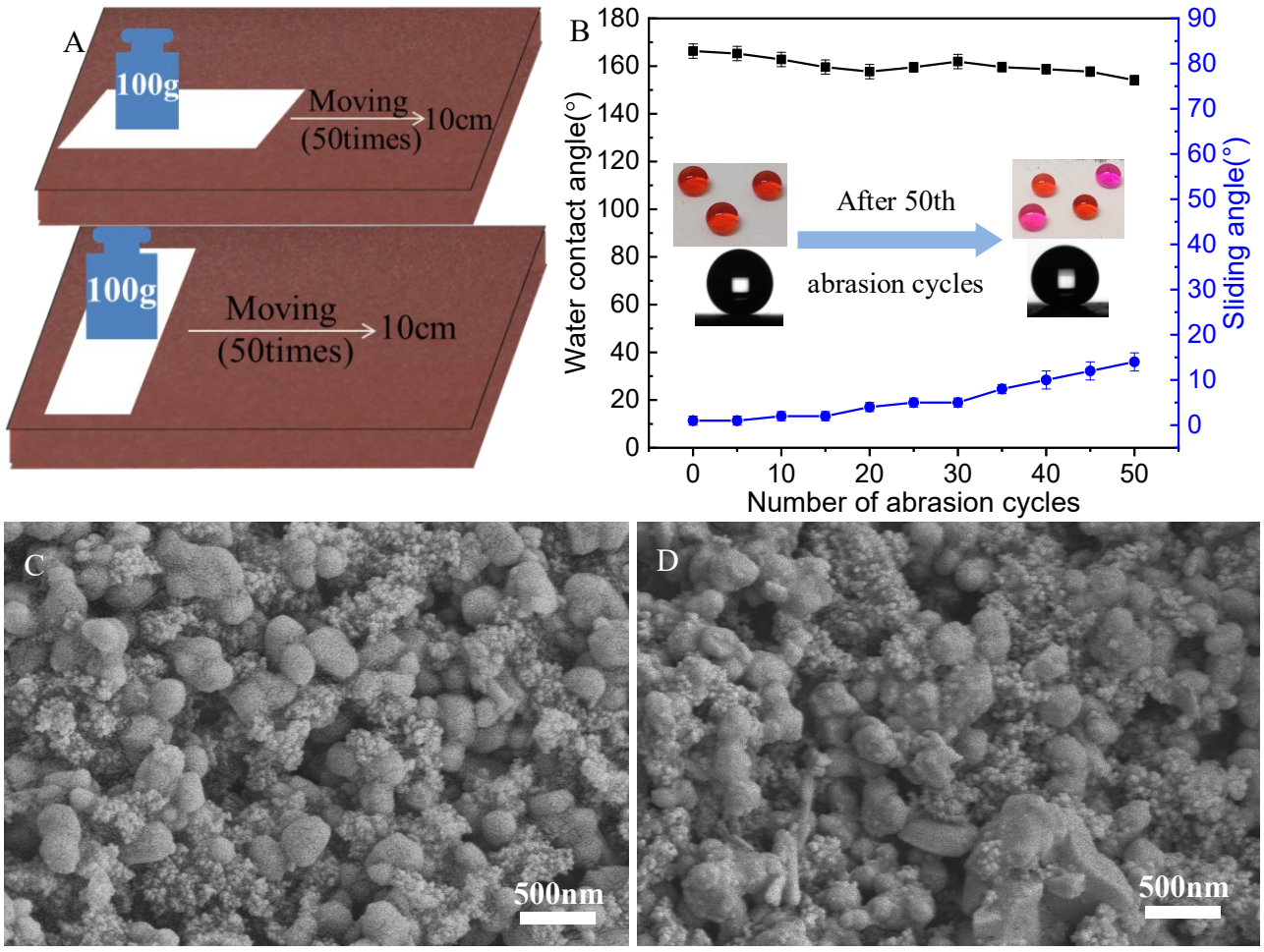
A
100g
Moving
(50times)
10cm
100g
Moving
(50times)
10cm
B
Water contact angle(°)
Sliding angle(°)
After 50th
abrasion cycles
Number of abrasion cycles
C
500nm
D
500nm

Fig.5.

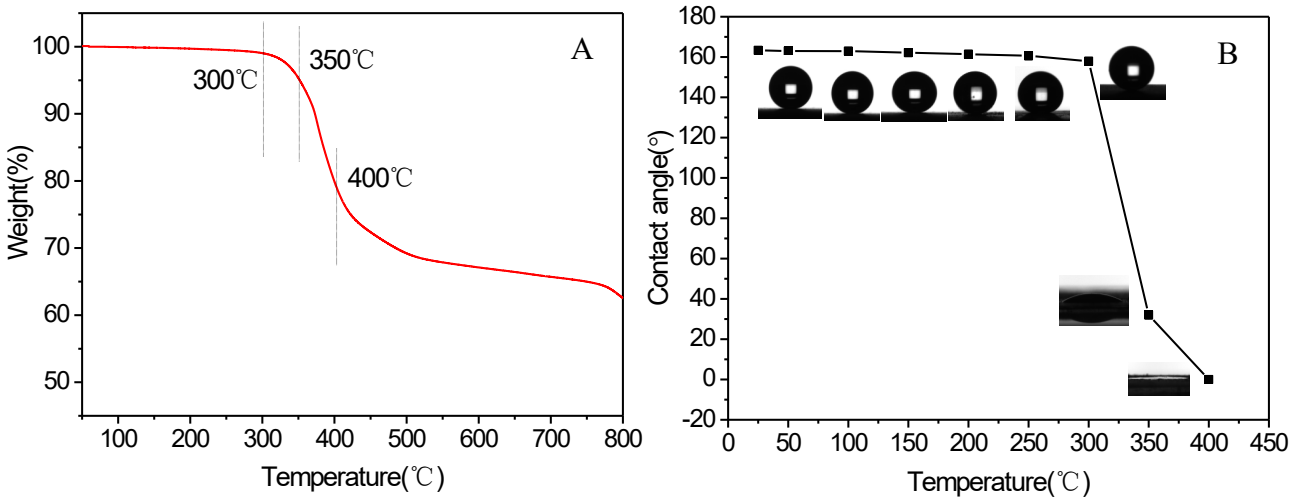
A
300℃
350℃
400℃
Weight(%)
Temperature(℃)
B
Contact angle(°)
Temperature(℃)

Fig.6.

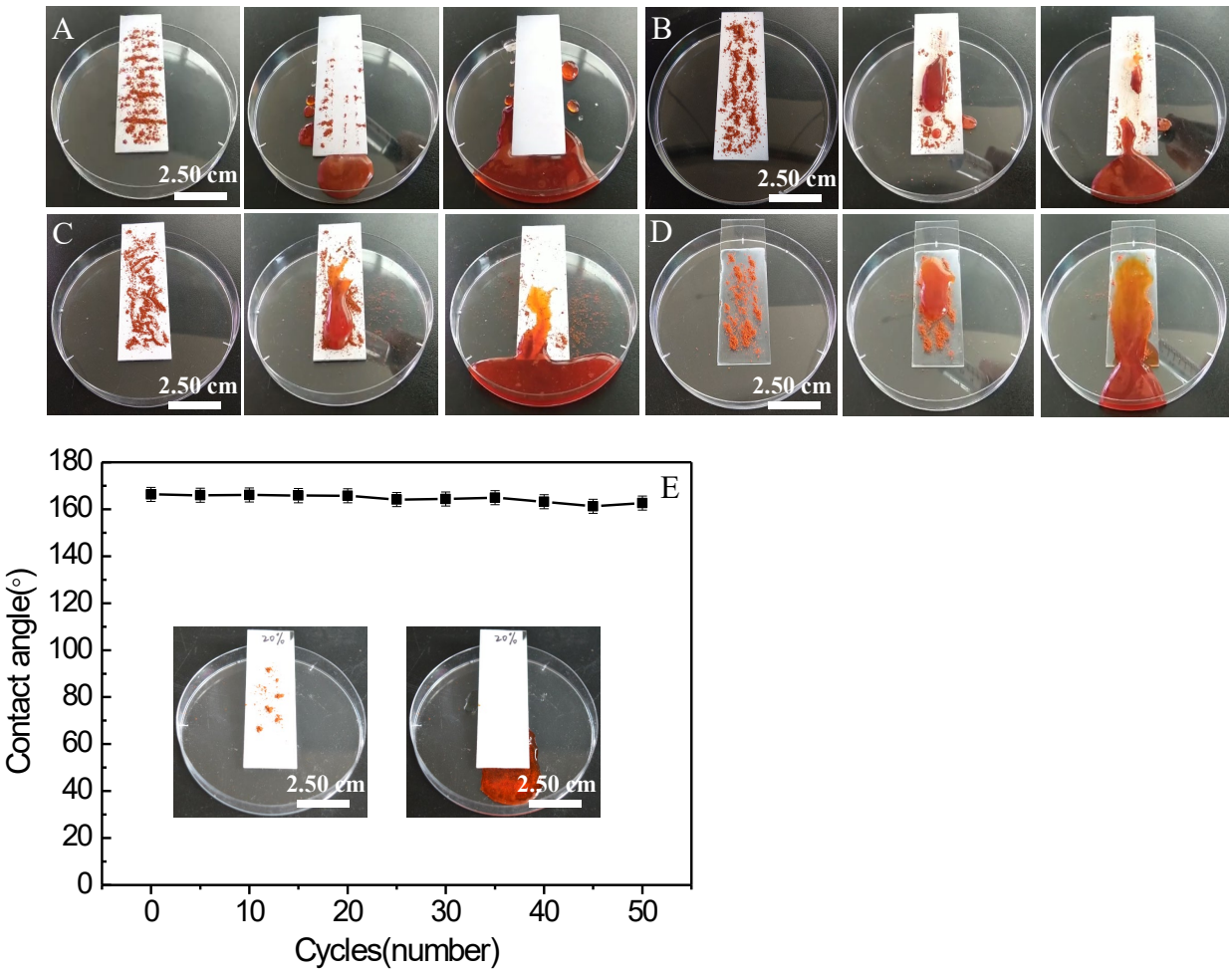
A
2.50 cm
B
2.50 cm
C
2.50 cm
D
2.50 cm
E
Contact angle(°)
Cycles(number)
0
10
20
30
40
50
0
20
40
60
80
100
120
140
160
180
2.50 cm
2.50 cm

Fig.7.

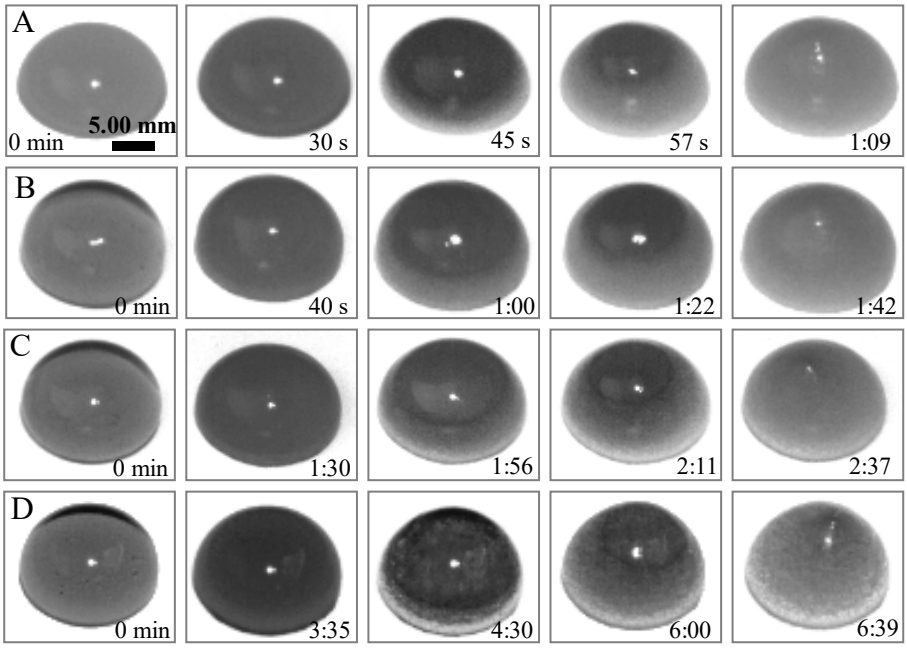
A
5.00 mm
0 min
30 s
45 s
57 s
1:09
B
0 min
40 s
1:00
1:22
1:42
C
0 min
1:30
1:56
2:11
2:37
D
0 min
3:35
4:30
6:00
6:39

Fig.8.

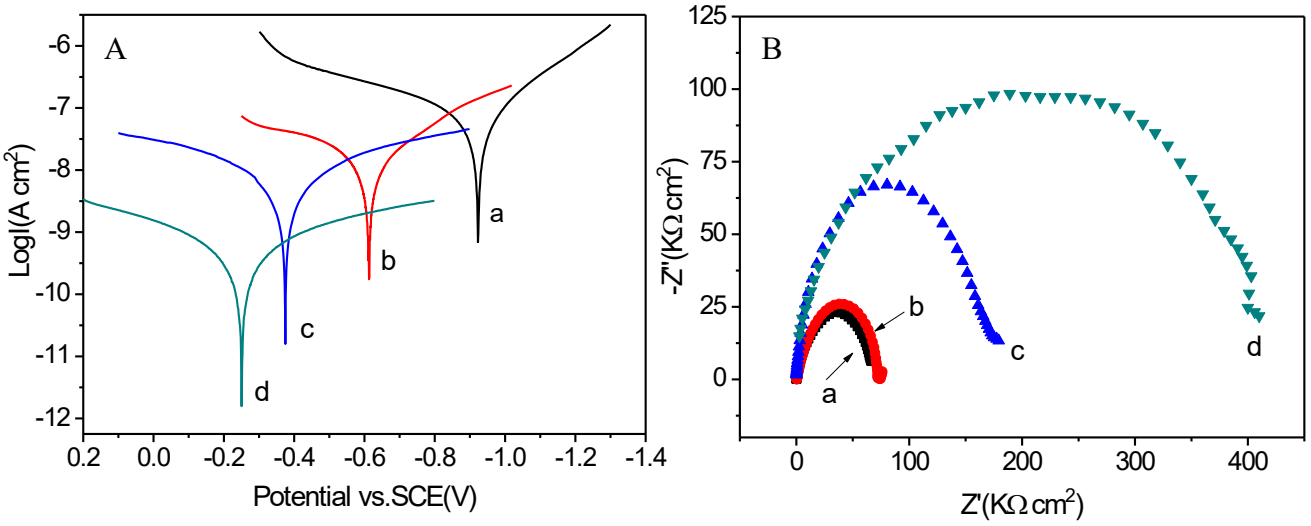
A
B
a
b
c
d
LogI(A cm^2)
Potential vs.SCE(V)
-Z''(KΩ cm^2)
Z'(KΩ cm^2)
-6
-7
-8
-9
-10
-11
-12
0.2
0.0
-0.2
-0.4
-0.6
-0.8
-1.0
-1.2
-1.4
125
100
75
50
25
0
0
100
200
300
400

Fig.9.